Tunable Van Hove Singularity without Structural Instability in Kagome Metal math xmlns="http://www.w3.org/1998/Math/MathML" display="inline">mrow>msub>mrow>mi>CsTi/mi>/mrow>mrow>mn>3/mn>/mrow>/msub>/mrow>mrow>msub>mrow>mi>Bi/mi>/mrow>mrow>mn>5/mn>/mrow>/msub>/mrow>/math>

Bo Liu et al.

Phys. Rev. Lett. **131**, 026701 — Published 12 July 2023

DOI: 10.1103/PhysRevLett.131.026701

Tunable van Hove singularity without structural instability in Kagome metal $CsTi_3Bi_5$

Bo Liu[1,#], Minquan Kuang[2,#], Yang Luo[1,#], Yongkai Li[3,4,#], Cheng Hu[5], Jiarui Liu[1,6], Qian Xiao[7], Xiquan Zheng[7], Linwei Huai[1], Shuting Peng[1], Zhiyuan Wei[1], Jianchang Shen[1], Bingqian Wang[1], Yu Miao[1], Xiupeng Sun[1], Zhipeng Ou[1], Shengtao Cui[8], Zhe Sun[8], Makoto Hashimoto[9], Donghui Lu[9], Chris Jozwiak[10], Aaron Bostwick[10], Eli Rotenberg[10], Luca Moreschini[5,11], Alessandra Lanzara[5,11], Yao Wang[6], Yingying Peng[7], Yugui Yao[3,4], Zhiwei Wang[3,4,12,*] and Junfeng He[1,*]

[1]*Department of Physics and CAS Key Laboratory of Strongly-coupled Quantum Matter Physics, University of Science and Technology of China, Hefei, Anhui 230026, China*

[2]*Chongqing Key Laboratory of Micro & Nano Structure Optoelectronics, and School of Physical Science and Technology, Southwest University, Chongqing 400715, China*

[3]*Centre for Quantum Physics, Key Laboratory of Advanced Optoelectronic Quantum Architecture and Measurement (MOE), School of Physics, Beijing Institute of Technology, Beijing 100081, China*

[4]*Beijing Key Lab of Nanophotonics and Ultrafine Optoelectronic Systems, Beijing Institute of Technology, Beijing 100081, China*

[5]*Material Sciences Division, Lawrence Berkeley National Laboratory, Berkeley, California 94720, USA*

[6]*Department of Physics and Astronomy, Clemson University, Clemson, South Carolina 29631, USA*

[7]*International Center for Quantum Materials, School of Physics, Peking University, Beijing 100871, China*

[8]*National Synchrotron Radiation Laboratory, University of Science and Technology of China, Hefei, Anhui 230026, China*

[9]*Stanford Synchrotron Radiation Lightsource, SLAC National Accelerator Laboratory, Menlo Park, California 94025, USA*

[10]*Advanced Light Source, Lawrence Berkeley National Laboratory, Berkeley, California 94720, USA*

[11]*Department of Physics, University of California, Berkeley, Berkeley, California 94720, USA*

[12]*Material Science Center, Yangtze Delta Region Academy of Beijing Institute of Technology, Jiaxing, 314011, China*

[#]These authors contributed equally to this work. *To whom correspondence should be addressed: J.H. (jfhe@ustc.edu.cn), Z.W.(zhiweiwang@bit.edu.cn)

In Kagome metal CsV_3Sb_5, multiple intertwined orders are accompanied by both electronic and structural instabilities. These exotic orders have attracted much recent attention, but their origins remain elusive. The newly discovered $CsTi_3Bi_5$ is a Ti-based Kagome metal to parallel CsV_3Sb_5. Here, we report angle-resolved photoemission experiments and first-principles calculations on pristine and Cs-doped $CsTi_3Bi_5$ samples. Our results reveal that the van Hove singularity (vHS) in $CsTi_3Bi_5$ can be tuned in a large energy range without structural instability, different from that in CsV_3Sb_5. As such, $CsTi_3Bi_5$ provides a complementary platform to disentangle and investigate the electronic instability with a tunable vHS in Kagome metals.

Kagome metals AV_3Sb_5 (A=K, Rb, Cs) have attracted much interest due to the coexistence of multiple exotic orders and states, ranging from superconductivity [1-3], charge density wave (CDW) [4-12], pair density wave [12], stripe order [4], nematic order [13,14], topologically nontrivial states [1,15] and time-reversal symmetry breaking states [11,16-18]. Despite the richness of these phenomena, their underlying mechanisms are still under debate. In principle, either electronic or structural instabilities of a material can drive the system into an ordered state with a lower energy. In AV_3Sb_5 (A=K, Rb, Cs), electronic instabilities are naturally provided by vHSs in the electron dispersion [19-22], and the structural instabilities are evidenced by the imaginary frequency in the phonon dispersion [23]. As a result, the explanations of the experimentally identified orders are often controversial. For example, the CDW order in AV_3Sb_5 (A=K, Rb, Cs) has been attributed to either electronic nesting between vHSs [22-25] or electron-phonon coupling [26-30]; the rotational symmetry breaking has been associated with either electronic nematicity [13,14,31] or lattice modulation [14,31]. The coexisted instabilities in both electron and lattice degrees of freedom make it very challenging to identify the primary driving mechanism for the various orders in AV_3Sb_5 (A=K, Rb, Cs). In this regard, the importance of comparative studies in a parallel material system is clear. Theoretical calculations have predicted dozens of materials, which are similar to AV_3Sb_5 (A=K, Rb, Cs) [32,33]. However, ATi_3Bi_5 (A=Cs, Rb) is the only material family that has been successfully synthesized recently [34,35].

In this Letter, we investigate pristine and Cs surface doped $CsTi_3Bi_5$ samples by angle-resolved photoemission spectroscopy (ARPES) measurements and first-principles calculations. The band structure of $CsTi_3Bi_5$ is clearly revealed, which shows a clear resemblance to the calculated results.

The vHS is well above Fermi level (E_F) in the pristine $CsTi_3Bi_5$. Surprisingly, the position of the vHS can be easily tuned in a large energy range by Cs surface doping. This property is distinct from that in CsV_3Sb_5, where the Cs surface doping primarily changes the electron-like band formed by Sb orbitals but has little effect on the vHS formed by V orbitals [36]. First-principles calculations further reveal the absence of structural instability in both pristine and electron doped $CsTi_3Bi_5$. This is also confirmed by our low-temperature X-ray diffraction measurements on the $CsTi_3Bi_5$ sample. As such, our results establish $CsTi_3Bi_5$ as a complementary material platform to CsV_3Sb_5, in which the electronic instability can be systematically examined without the interference from the lattice degree of freedom. These studies also provide new insights on the origin of CDW order and nematic order in the related Kagome metals.

Single crystals of $CsTi_3Bi_5$ were grown by a self-flux method with binary Cs-Bi as the flux. The raw materials were loaded in an alumina crucible and sealed in an evacuated quartz tube. The tube was heated slowly to 1000 °C and held for 12 h. It was then cooled down to 850°C at a rate of 10 °C /h and to 500°C at a rate of 3°C /h, at which the flux was removed by a centrifuge. The synchrotron-based ARPES measurements were performed at Advanced Light Source (ALS) beamline 7.0.2 and Stanford Synchrotron Radiation Lightsource (SSRL) beamline 5-2, with some preliminary tests at National Synchrotron Radiation Laboratory. ARPES measurements were also carried out at our lab-based ARPES system using 21.2eV photons with a total energy resolution of ~5meV and a base pressure of better than 5×10^{-11} torr. The Fermi level was determined by measuring a polycrystalline Au piece in electrical contact with the samples. First-principles calculations were performed by using the VASP software package. The details of the calculations and the related parameters are described in the supplemental material [37].

The crystal structure of $CsTi_3Bi_5$ is similar to that of CsV_3Sb_5 (Fig. 1a). The Ti sublattice forms a Kagome net, which is interwoven with a hexagonal net of Bi atoms in the same plane. The measured band structure of $CsTi_3Bi_5$ is shown in Fig. 1b, which bears a clear resemblance to that of the first-principles calculations (Fig. 1d). Due to the layered nature of the material, a projected in-plane Brillouin zone (BZ) is used for the description. The electronic structure near the $\bar{\Gamma}$ point is dominated by an electron-like band (labelled as α band, hereafter), giving rise to a circular Fermi surface sheet (Fig. 1c). Multiple hole-like bands are observed around the $\bar{M}$ point, which are labelled as β, γ and δ band, respectively (Fig. 1b, d). We note that the β and γ bands are very close to each other

below E_F (Fig. 1b), which can be better resolved when they are well separated in the doped sample (Fig. 2d). These hole-like bands are associated with the hexagonal, flower-like and diamond-like Fermi surface sheet, respectively (Fig. 1c). A Dirac-like crossing can be seen at $\bar{K}$ point well below E_F (Fig. 1b, d). A triangular Fermi surface sheet is observed around the $\bar{K}$ point (Fig. 1c). The characteristic vHS of the Kagome lattice is shown at $\bar{M}$ point in the calculation (Fig. 1d, indicated by the orange shade, the small energy gap is induced by the spin-orbit coupling). Nevertheless, the vHS locates at ~150 meV above E_F, which cannot be probed by the photoemission measurements (Fig. 1d).

After revealing the overall electronic structure of the $CsTi_3Bi_5$, we now investigate the doping evolution via *in situ* surface deposition of Cs atoms. As shown in Fig. 2a, the electron-like band (α band) around $\bar{\Gamma}$ exhibits a moderate change as a function of Cs doping. The bottom of the band shows a little movement in energy (also see supplemental Fig. S1). The distance between two Fermi momenta of this band (k_{F1} and k_{F2}) increases slightly with doping (Fig. 2a, b). On the contrary, the energy bands around the $\bar{M}$ point exhibit more significant changes as a function of the Cs doping (Fig. 2d, supplemental Fig. S1). In particular, the γ and δ bands present a clear downward shift, echoing the expected electron doping with Cs surface deposition. We note that the top of these hole-like bands starts to appear with sufficient Cs doping [Fig. 2d(v)], indicating that the vHS is in the vicinity of E_F. This is also evidenced by the enhanced electron density of states at E_F in this momentum region (Fig. 2e, f). The integrated energy distribution curve (EDC) around the $\bar{M}$ point shows a negligible peak in the pristine $CsTi_3Bi_5$ (Fig. 2e, doping sequence 0), as the vHS is well above E_F [Fig. 2d (i)]. However, the peak intensity increases significantly with Cs doping, demonstrating the boost of low energy electron density of states as the vHS approaches E_F (Fig. 2e, f). In order to quantitatively unveil the vHS, the Cs surface doping is reproduced at an elevated temperature (T=200K), where the thermal population of electrons enables a complete examination of the fine features around E_F. As shown in Fig. 3a-d, the vHS is indeed shifted downward with the Cs doping. On the sufficiently doped sample, the flat dispersion of the vHS can be clearly identified in the vicinity of E_F (Fig. 3b, d, also see supplemental Figs. S2 and S3). These results are quantitatively extracted from the raw data and summarized in Fig. 3f. Orbital-resolved calculations have also been carried out, which illustrate that the electron-like α band around $\bar{\Gamma}$ is dominated by Bi P_z orbital,

whereas the vHS is primarily associated with Ti $d_{x^2-y^2}/d_{xy}$ orbital (Fig. 3e). These observations have collectively depicted an integrated picture of orbital selective movements of the energy bands with Cs doping -- the vHS with Ti *d* orbitals can be tuned in a large energy range, whereas the electron-like α band with Bi *P* orbitals remains less sensitive to the doping process. This is distinct from the evolution in CsV_3Sb_5, where the vHS with V *d* orbitals shows little change with Cs surface doping, but the electron-like band with Sb *P* orbitals shifts ~240 meV in energy [36].

Next, we examine the lattice degree of freedom in the $CsTi_3Bi_5$ crystal. In CsV_3Sb_5, both Star of David (SD) and inverse Star of David (ISD) structures are considered to be more stable than the Kagome lattice. Therefore, we have followed the idea in CsV_3Sb_5 [23], and calculated the change of total energy in $CsTi_3Bi_5$, assuming that the lattice is breathing in and out towards the potential SD and ISD structures (Fig. 4a). Similar to the earlier report, either SD or ISD structure shows a lower total energy than that of the Kagome structure in CsV_3Sb_5 (Fig. 4b), leading to structural instabilities of the material [23]. On the contrary, the Kagome structure in $CsTi_3Bi_5$ exhibits the lowest total energy, demonstrating the absence of structural instability (Fig. 4c). This result remains solid when electron doping is considered in the $CsTi_3Bi_5$ system (Fig. 4d). Phonon spectra are also calculated for both pristine and electron doped $CsTi_3Bi_5$ (Fig. 4e). The absence of imaginary frequency echoes a stable Kagome structure in $CsTi_3Bi_5$. In addition, we have carried out low-temperature X-ray diffraction measurement on $CsTi_3Bi_5$ (Fig. 4f), which also confirms the Kagome structure without any super-modulation of the lattice.

Finally, we discuss the implications of our observations. The tunable vHS and the absence of structural instabilities make $CsTi_3Bi_5$ a complementary material platform to compare with CsV_3Sb_5. In CsV_3Sb_5, the existence of electronic and structural instabilities give rise to various emergent phenomena. However, their coexistence also makes it hard to differentiate the primary driving mechanism for the different phenomena. In $CsTi_3Bi_5$, without the interference from the lattice, one can systematically examine the electronic instabilities. For example, the CDW order is absent in pristine $CsTi_3Bi_5$ [34,35], and no CDW gap is observed in our ARPES measurements (supplemental Fig. S4). This could be attributed to either the absence of electronic nesting condition or the absence of imaginary frequency in the phonon spectra. However, when the vHS is tuned to the vicinity of E_F, the photoemission spectra remain gapless at low temperature (supplemental Fig. S5). There results indicate that the electronic nesting between vHSs at $\bar{M}$ points alone is insufficient to drive a CDW

order in the Kagome metal. This point can also be illustrated by the zero-frequency joint density of states [22,38] calculated from the autocorrelation of the measured Fermi surface, where a peak appears at M point (nesting between vHSs) in both CsV_3Sb_5 and Cs doped $CsTi_3Bi_5$, but disappears in the pristine $CsTi_3Bi_5$ (see supplemental Figs. S6-7). In order to understand the origin, we have calculated the charge susceptibility in $CsTi_3Bi_5$ (see supplemental Fig. S8). A finite peak does appear at M point when the Fermi level is at the vHS. However, an unreasonably large Coulomb interaction is required to drive the CDW transition when pure electronic interactions are considered. In this context, the structural instabilities in CsV_3Sb_5 may play an essential role in driving the CDW order. This is also supported by our calculations showing that the CDW transition as a function of doping is determined by the total energy of the system (see supplemental Fig. S9). Nevertheless, the electronic correlation in CsV_3Sb_5 may contribute to the unconventional behaviors of the CDW orders, although a structural instability seems to be important to trigger the phase transition. On the other hand, nematic order reported in $CsTi_3Bi_5$ [39,40] can only be driven by pure electronic interactions. Our DFT calculations and X-ray diffraction measurement illustrate that the lattice of $CsTi_3Bi_5$ reserves 6-fold symmetry (Fig. 4f and supplemental Figs. S10-11), whereas our polarization dependent ARPES measurements point to the existence of orbital hybridization (supplemental Figs. S12-13), echoing the theoretical proposal of a rotational symmetry breaking hybridizations among different orbitals [39,40]. In this context, it would be interesting to further explore how the tunable vHS in $CsTi_3Bi_5$ would interact with the nematic order and other potential electronic orders in the system.

In summary, we have revealed the electronic structure of pristine and Cs surface doped $CsTi_3Bi_5$ samples. The Cs deposition induces an overall electron doping to the material, but the energy bands exhibit an orbital dependent movement with doping. Among them, the vHS can be tuned in a large energy range. First-principles calculations demonstrate that the Kagome structure remains stable in both pristine and electron doped $CsTi_3Bi_5$. These results establish a unique path to disentangle the electronic instability from that of the lattice, and to examine its relationship with the various exotic phenomena in Kagome metals.

We thank Y. Han, T. Wu, Z. Xiang, Z. Wang, I. Zeljkovic and H. Chen for useful discussions. The work at University of Science and Technology of China (USTC) was supported by the National Natural Science Foundation of China (Nos. 52273309, 12074358, 52261135638), the Fundamental Research

Funds for the Central Universities (Nos. WK3510000012, WK2030000035), the Innovation Program for Quantum Science and Technology (No. 2021ZD0302802) and the USTC start-up fund. The work at Southwest University was supported by the Natural Science Foundation of China (Grant No. 11704315). The work at Beijing Institute of Technology was supported by the National Key R&D Program of China (Grant Nos. 2020YFA0308800, 2022YFA1403400), the Natural Science Foundation of China (Grant No. 92065109), the Beijing Natural Science Foundation (Grant Nos. Z210006, Z190006). This work used resources of the Advanced Light Source, a US Department of Energy (DOE) Office of Science User Facility under contract No. DE-AC02-05CH11231. This work also acknowledges support by the U.S. Department of Energy, Office of Science, Office of Basic Energy Sciences, Materials Sciences and Engineering Division under Contract No. DE-AC02- 05CH11231 (Ultrafast Materials Science Program KC2203). Use of the Stanford Synchrotron Radiation Lightsource, SLAC National Accelerator Laboratory, is supported by the U.S. Department of Energy, Office of Science, Office of Basic Energy Sciences under Contract No. DE-AC02-76SF00515. Y.Y.P. is grateful for financial support from the National Natural Science Foundation of China (11974029). J.H. and Y.L. thank the Analysis & Testing Center at USTC for the support. Z.W. thanks the Analysis & Testing Center at BIT for assistance in facility support.

[1] B. R. Ortiz, S. M. L. Teicher, Y. Hu, J. L. Zuo, P. M. Sarte, E. C. Schueller, A. M. M. Abeykoon, M. J. Krogstad, S. Rosenkranz, R. Osborn, R. Seshadri, L. Balents, J. He, and S. D. Wilson, Phys. Rev. Lett. **125**, 247002 (2020).

[2] B. R. Ortiz, P. M. Sarte, E. M. Kenney, M. J. Graf, S. M. L. Teicher, R. Seshadri, and S. D. Wilson, Phys. Rev. Mater. **5**, 034801 (2021).

[3] Q. Yin, Z. Tu, C. Gong, Y. Fu, S. Yan, and H. Lei, Chin. Phys. Lett. **38**, 037403 (2021).

[4] H. Zhao, H. Li, B. R. Ortiz, S. M. L. Teicher, T. Park, M. Ye, Z. Wang, L. Balents, S. D. Wilson, and I. Zeljkovic, Nature (London) **599**, 216-221 (2021).

[5] Z. Liang, X. Hou, F. Zhang, W. Ma, P. Wu, Z. Zhang, F. Yu, J.-J. Ying, K. Jiang, L. Shan, Z. Wang, and X.-H. Chen, Phys. Rev. X **11**, 031026 (2021).

[6] H. Li, T. T. Zhang, T. Yilmaz, Y. Y. Pai, C. E. Marvinney, A. Said, Q. W. Yin, C. S. Gong, Z. J. Tu, E. Vescovo, C. S. Nelson, R. G. Moore, S. Murakami, H. C. Lei, H. N. Lee, B. J. Lawrie, and H. Miao, Phys. Rev. X **11**, 031050 (2021).

[7] B. R. Ortiz, S. M. L. Teicher, L. Kautzsch, P. M. Sarte, N. Ratcliff, J. Harter, J. P. C. Ruff, R. Seshadri, and S. D. Wilson, Phys. Rev. X **11**, 041030 (2021).

[8] F. H. Yu, D. H. Ma, W. Z. Zhuo, S. Q. Liu, X. K. Wen, B. Lei, J. J. Ying, and X. H. Chen, Nat. Commun. **12**, 3645 (2021).

[9] Y. Song, T. Ying, X. Chen, X. Han, X. Wu, A. P. Schnyder, Y. Huang, J.-G. Guo, and X. Chen, Phys. Rev. Lett. **127**, 237001 (2021).

[10] B. Q. Song, X. M. Kong, W. Xia, Q. W. Yin, C. P. Tu, C. C. Zhao, D. Z. Dai, K. Meng, Z. C. Tao, Z. J. Tu, C. S. Gong, H. C. Lei, Y. F. Guo, X. F. Yang, and S. Y. Li, arXiv:2105.09248 (2021).

[11] Y.-X. Jiang, J.-X. Yin, M. M. Denner, N. Shumiya, B. R. Ortiz, G. Xu, Z. Guguchia, J. He, M. S. Hossain, X. Liu, J. Ruff, L. Kautzsch, S. S. Zhang, G. Chang, I. Belopolski, Q. Zhang, T. A. Cochran, D. Multer, M. Litskevich, Z.-J. Cheng, X. P. Yang, Z. Wang, R. Thomale, T. Neupert, S. D. Wilson, and M. Z. Hasan, Nat. Mater. **20**, 1353-1357 (2021).

[12] H. Chen, H. Yang, B. Hu, Z. Zhao, J. Yuan, Y. Xing, G. Qian, Z. Huang, G. Li, Y. Ye, S. Ma, S. Ni, H. Zhang, Q. Yin, C. Gong, Z. Tu, H. Lei, H. Tan, S. Zhou, C. Shen, X. Dong, B. Yan, Z. Wang, and H.-J. Gao, Nature (London) **599**, 222-228 (2021).

[13] L. Nie, K. Sun, W. Ma, D. Song, L. Zheng, Z. Liang, P. Wu, F. Yu, J. Li, M. Shan, D. Zhao, S. Li, B. Kang, Z. Wu, Y. Zhou, K. Liu, Z. Xiang, J. Ying, Z. Wang, T. Wu, and X. Chen, Nature (London) **604**, 59-64 (2022).

[14] Y. Xiang, Q. Li, Y. Li, W. Xie, H. Yang, Z. Wang, Y. Yao, and H.-H. Wen, Nat. Commun. **12**, 6727 (2021).

[15] Y. Hu, S. M. L. Teicher, B. R. Ortiz, Y. Luo, S. Peng, L. Huai, J. Ma, N. C. Plumb, S. D. Wilson, J. He, and M. Shi, Sci. Bull. **67**, 495 (2022).

[16] C. M. III, D. Das, J.-X. Yin, H. Liu, R. Gupta, Y.-X. Jiang, M. Medarde, X. Wu, H. C. Lei, J. Chang, P. Dai, Q. Si, H. Miao, R. Thomale, T. Neupert, Y. Shi, R. Khasanov, M. Z. Hasan, H. Luetkens, and Z. Guguchia, Nature (London) **602**, 245-250 (2022).

[17] L. Yu, C. Wang, Y. Zhang, M. Sander, S. Ni, Z. Lu, S. Ma, Z. Wang, Z. Zhao, H. Chen, K. Jiang, Y. Zhang, H. Yang, F. Zhou, X. Dong, S. L. Johnson, M. J. Graf, J. Hu, H.-J. Gao, and Z. Zhao, arXiv:2107.10714 (2021).

[18] R. Khasanov, D. Das, R. Gupta, C. Mielke III, M. Elender, Q. Yin, Z. Tu, C. Gong, H. Lei, E. T. Ritz, R. M. Fernandes, T. Birol, Z. Guguchia, and H. Luetkens, Phys. Rev. Res. **4**, 023244 (2022).

[19] M. Kang, S. Fang, J.-K. Kim, B. R. Ortiz, S. H. Ryu, J. Kim, J. Yoo, G. Sangiovanni, D. D. Sante, B.-G. Park, C. Jozwiak, A. Bostwick, E. Rotenberg, E. Kaxiras, S. D. Wilson, J.-H. Park, and R. Comin, Nat. Phys. **18**, 301-308 (2022).

[20] Y. Hu, X. Wu, B. R. Ortiz, S. Ju, X. Han, J. Ma, N. C. Plumb, M. Radovic, R. Thomale, S. D. Wilson, A. P. Schnyder, and M. Shi, Nat. Commun. **13**, 2220 (2022).

[21] Z. Liu, N. Zhao, Q. Yin, C. Gong, Z. Tu, M. Li, W. Song, Z. Liu, D. Shen, Y. Huang, K. Liu, H. Lei, and S. Wang, Phys. Rev. X **11**, 041010 (2021).

[22] S. Cho, H. Ma, W. Xia, Y. Yang, Z. Liu, Z. Huang, Z. Jiang, X. Lu, J. Liu, Z. Liu, J. Li, J. Wang, Y. Liu, J. Jia, Y. Guo, J. Liu, and D. Shen, Phys. Rev. Lett. **127**, 236401 (2021).

[23] H. Tan, Y. Liu, Z. Wang, and B. Yan, Phys. Rev. Lett. **127**, 046401 (2021).

[24] R. Lou, A. Fedorov, Q. Yin, A. Kuibarov, Z. Tu, C. Gong, E. F. Schwier, B. Buchner, H. Lei, and S. Borisenko, Phys. Rev. Lett. **128**, 036402 (2022).

[25] X. Zhou, Y. Li, X. Fan, J. Hao, Y. Dai, Z. Wang, Y. Yao, and H.-H. Wen, Phys. Rev. B **104**, L041101 (2021).

[26] H. Luo, Q. Gao, H. Liu, Y. Gu, D. Wu, C. Yi, J. Jia, S. Wu, X. Luo, Y. Xu, L. Zhao, Q. Wang, H. Mao, G. Liu, Z. Zhu, Y. Shi, K. Jiang, J. Hu, Z. Xu, and X. J. Zhou, Nat. Commun. **13**, 273 (2022).

[27] E. Uykur, B. R. Ortiz, S. D. Wilson, M. Dressel, and A. A. Tsirlin, npj Quantum Mater. **7**, 16 (2022).

[28] Y. Xie, Y. Li, P. Bourges, A. Ivanov, Z. Ye, J.-X. Yin, M. Z. Hasan, A. Luo, Y. Yao, Z. Wang, G. Xu, and P. Dai, Phys. Rev. B **105**, L140501 (2022).

[29] Z. Ye, A. Luo, J.-X. Yin, M. Z. Hasan, and G. Xu, Phys. Rev. B **105**, 245121 (2022).

[30] M. Wenzel, B. R. Ortiz, S. D. Wilson, M. Dressel, A. A. Tsirlin, and E. Uykur, arXiv:2112.07501 (2021).

[31] Z. Jiang, H. Ma, W. Xia, Q. Xiao, Z. Liu, Z. Liu, Y. Yang, J. Ding, Z. Huang, J. Liu, Y. Qiao, J. Liu, Y. Peng, S. Cho, Y. Guo, J. Liu, and D. Shen, arXiv:2208.01499 (2022).

[32] Y. Jiang, Z. Yu, Y. Wang, T. Lu, S. Meng, K. Jiang, and M. Liu, Chin. Phys. Lett. **39**, 047402 (2022).

[33] X.-W. Yi, X.-Y. Ma, Z. Zhang, Z.-W. Liao, J.-Y. You, and G. Su, arXiv:2202.05588 (2022).

[34] H. Yang, Z. Zhao, X.-W. Yi, J. Liu, J.-Y. You, Y. Zhang, H. Guo, X. Lin, C. Shen, H. Chen, X. Dong, G. Su, and H.-J. Gao, arXiv:2209.03840 (2022).

[35] D. Werhahn, B. R. Ortiz, A. K. Hay, S. D. Wilson, R. Seshadri, and D. Johrendt, Zeitschrift für Naturforsch. B online (2022). doi:10.1515/znb-2022-0125.

[36] K. Nakayama, Y. Li, T. Kato, M. Liu, Z. Wang, T. Takahashi, Y. Yao, and T. Sato, Phys. Rev. X **12**, 011001 (2022).

[37] See Supplemental Material [url] for the details of the theoretical calculations and other supporting information, which includes Refs. [23, 28, 41-48].

[38] Z. Jiang, Z. Liu, H. Ma, W. Xia, Z. Liu, J. Liu, S. Cho, Y. Yang, J. Ding, J. Liu, Z. Huang, Y. Qiao, J. Shen, W. Jing, X. Liu, J. Liu, Y. Guo, and D. Shen, arXiv:2212.02399 (2022).

[39] H. Yang, Y. Ye, Z. Zhao, J. Liu, X.-W. Yi, Y. Zhang, J. Shi, J.-Y. You, Z. Huang, B. Wang, J. Wang, H. Guo, X. Lin, C. Shen, W. Zhou, H. Chen, X. Dong, G. Su, Z. Wang, and H.-J. Gao, arXiv:2211.12264 (2022).

[40] H. Li, S. Cheng, B. R. Ortiz, H. Tan, D. Werhahn, K. Zeng, D. Jorhendt, B. Yan, Z. Wang, S. D. Wilson, and I. Zeljkovic, arXiv:2211.16477 (2022).

[41] M. D. Johannes, I. I. Mazin, and C. A. Howells, Phys. Rev. B **73**, 205102 (2006).

[42] G. Kresse and J. Hafner, Phys. Rev. B **48**, 13115 (1993).

[43] G. Kresse and J. Furthmüller, Comput. Mater. Sci. **6**, 15 (1996).

[44] P. E. Blöchl, Phys. Rev. B **50**, 17953 (1994).

[45] J. P. Perdew, K. Burke, and M. Ernzerhof, Phys. Rev. Lett. **77**, 3865 (1996); **78**, 1396 (1997).

[46] S. Grimme, J. Antony, S. Ehrlich, and H. Krieg, J. Chem. Phys. **132**, 154104 (2010).

[47] A. Togo, and I. Tanaka, Scr. Mater. **108**, 1 (2015).

[48] Q. S. Wu, S. Zhang, H. F. Song, M. Troyer, and A. A. Soluyanov, Comput. Phys. Commun. **224**, 405 (2018).

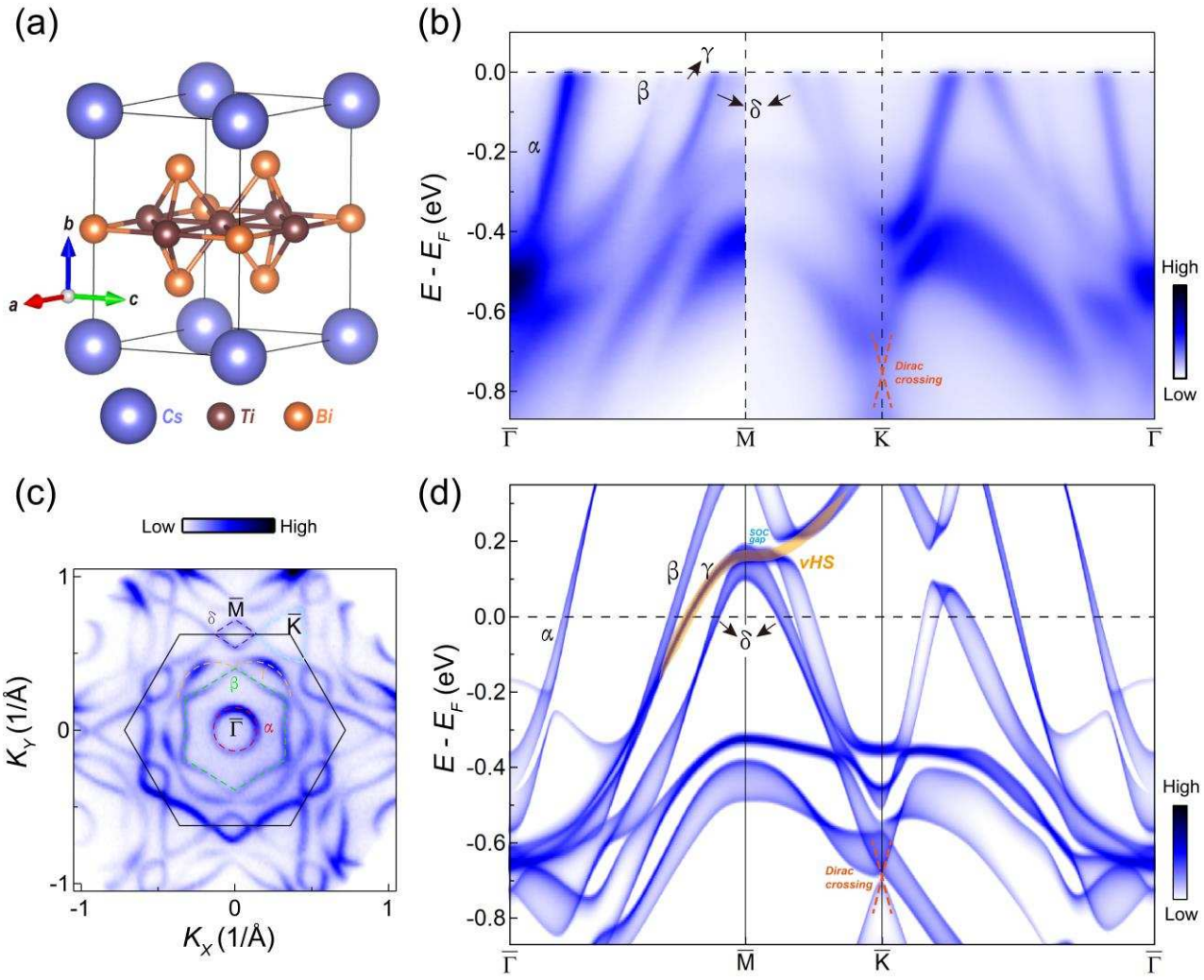

FIG. 1. Electronic structure of $CsTi_3Bi_5$. (a) Crystal structure of $CsTi_3Bi_5$. (b-c) Photoelectron intensity plot of the band structure along the $\bar{\Gamma}$-$\bar{M}$-$\bar{K}$-$\bar{\Gamma}$ direction (b) and the Fermi surface (c) of $CsTi_3Bi_5$ measured with 78 eV photons at 7 K. The dashed lines in (c) are an eye-guide for the different Fermi surface sheets. (d) The bulk band structure of $CsTi_3Bi_5$ obtained from first-principles calculations with spin-orbit coupling included. The electron-like band around $\bar{\Gamma}$ and the hole-like bands near $\bar{M}$ are labelled as α, β, γ and δ band, respectively. The orange shade is an eye-guide for the vHS.

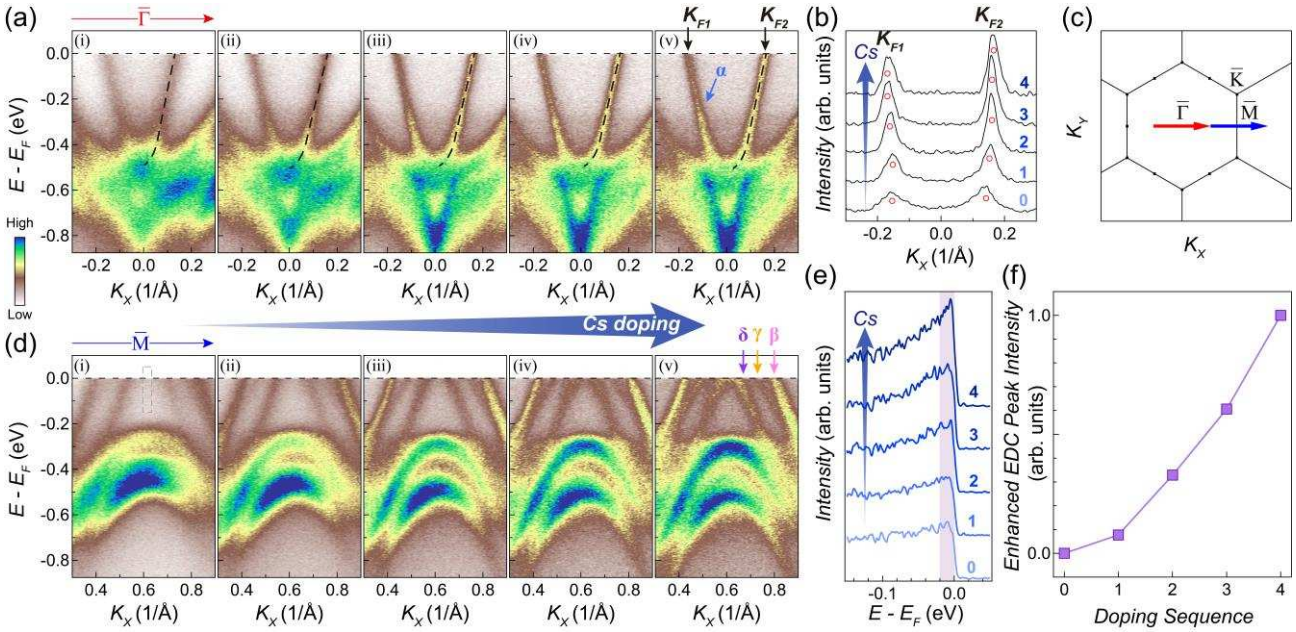

FIG. 2. Evolution of the electronic structure with Cs surface doping at 7K. (a) Photoelectron intensity plot of the band structure around $\bar{\Gamma}$ (along the $\bar{M}$-$\bar{\Gamma}$-$\bar{M}$ direction) as a function of continuous Cs doping on the same sample, measured with 21.2 eV photons. The results at doping sequences 0-4 are shown in (i-v), respectively. Doping sequence 0 indicates the pristine $CsTi_3Bi_5$ sample. The dashed lines are a guide to the eye. (b) Momentum distribution curves (MDCs) at E_F extracted from (a). The numbers 0-4 denote the doping sequences. (c) The projected in-plane BZ and the momentum locations of the cuts. (d) Same as (a), but for the band structure around $\bar{M}$ (along the $\bar{\Gamma}$-$\bar{M}$-$\bar{\Gamma}$ direction). (e) Integrated EDC around the $\bar{M}$ point in (d). The integration window is marked by the gray dashed box in the first panel of (d). The numbers 0-4 denote the doping sequences. (f) Enhanced EDC peak intensity around $\bar{M}$ as a function of the doping sequence. The absolute EDC peak intensity at the doping sequence x (x=0-4) is calculated by integrating the area between -20meV and E_F [the pink shaded region in (e)] of the corresponding EDC, and labelled as I_x. The enhanced EDC peak intensity is defined as $(I_x-I_0)/(I_4-I_0)$.

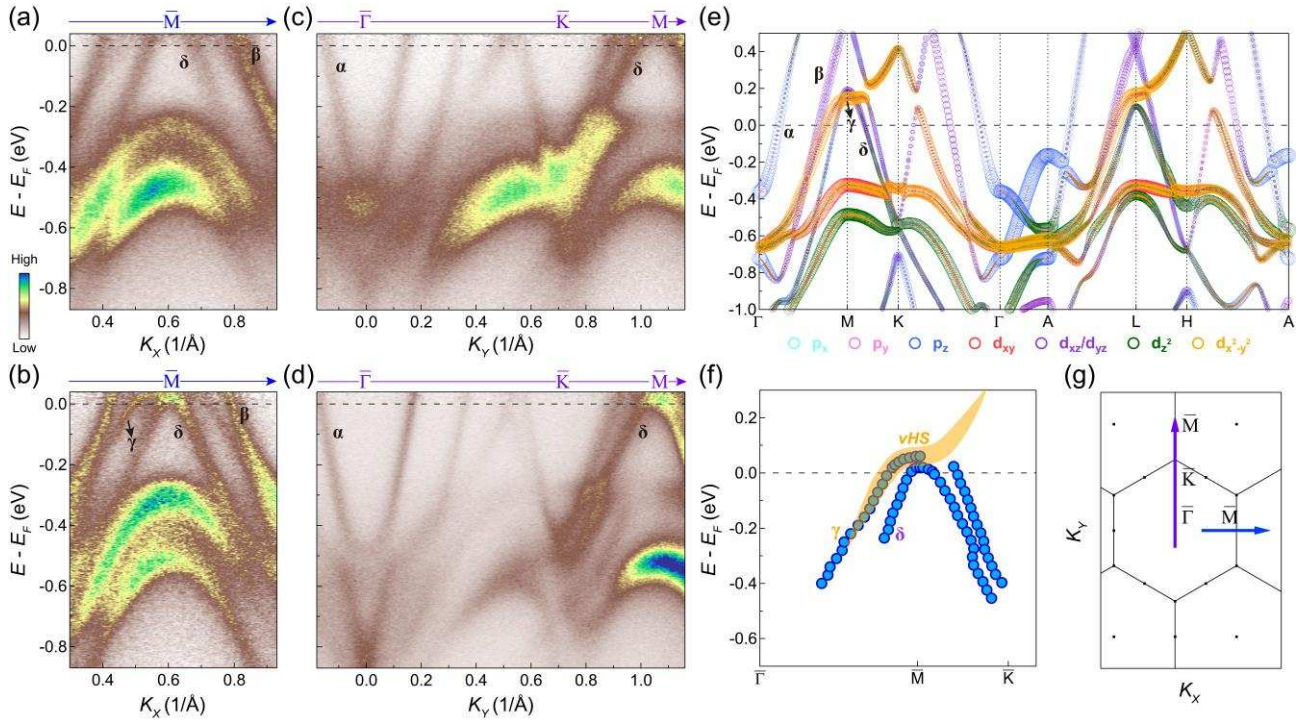

FIG. 3. Doping evolution of the vHS. (a-b) Photoelectron intensity plot of the band structure around $\bar{M}$ (along the $\bar{\Gamma}$-$\bar{M}$-$\bar{\Gamma}$ direction) before (a) and after (b) the Cs surface doping, measured with 21.2 eV photons at 200 K. (c-d) Same as (a-b), but measured along the $\bar{\Gamma}$-$\bar{K}$-$\bar{M}$ direction. (e) Orbital-resolved band structure obtained by first-principles calculations. Different orbitals are presented in different colors. The size of the markers represents the spectral weight of the orbitals. (f) Quantified dispersion of the γ and δ bands near $\bar{M}$ after the sufficient Cs doping, extracted from (b) and (d). The orange shade is an eye-guide for the vHS. (g) The projected in-plane BZ and the momentum locations of the cuts.

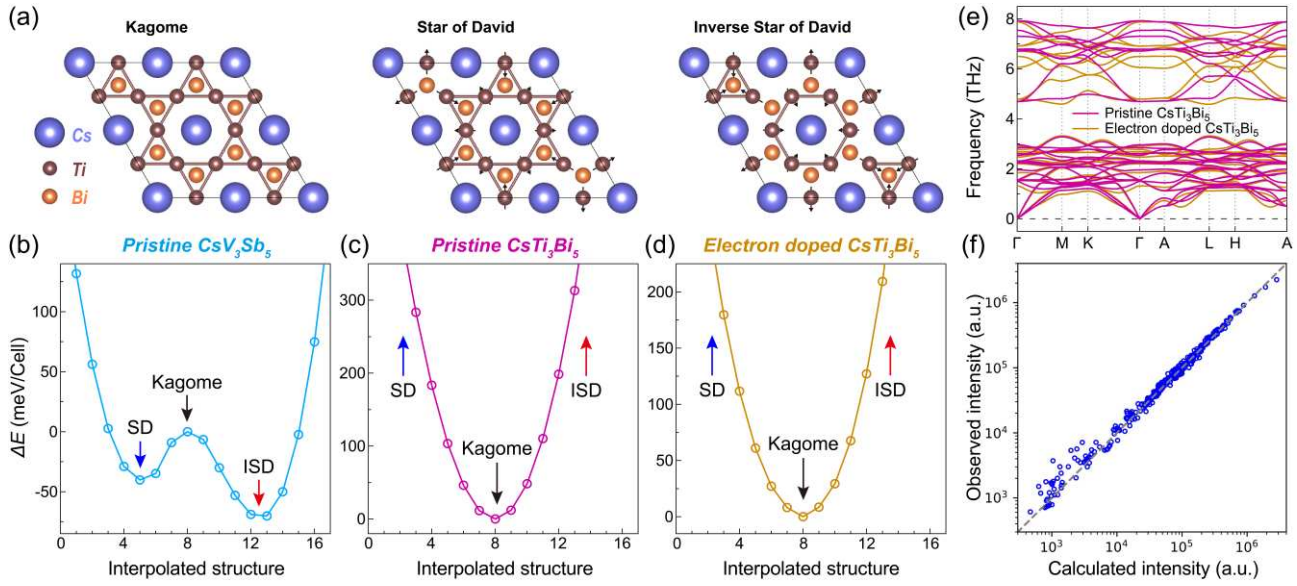

FIG. 4. Calculated total energy profiles, phonon spectra and X-ray diffraction measurements. (a) The 2×2x1 supercells for Kagome structure, Star of David structure and Inverse Star of David structure. The black arrows indicate the lattice distortion due to the breathing mode. (b-d) Total energy as a function of the interpolated structure in pristine CsV_3Sb_5 (b), pristine $CsTi_3Bi_5$ (c), and electron doped $CsTi_3Bi_5$ (d). The ΔE stands for the relative total energy with respect to the Kagome structure per supercell (36 atoms). (e) Calculated phonon spectra along the high-symmetry directions in pristine $CsTi_3Bi_5$ (magenta line) and electron doped $CsTi_3Bi_5$ (orange line). (f) Comparison between the observed X-ray diffraction intensities from 322 indexed Bragg peaks measured at 18K and the calculation from the crystal structure of $CsTi_3Bi_5$ with the space group of P6/mmm.